







Frequency-dependent surface wave suppression at the Dirac point of an acoustic graphene analog

Nicholas T. Gangemi ^{1,2,*}, Caleb F. Sieck,³ Joseph F. Vignola,² Diego Turo ², Alec Ikei ³,
Amelia Vignola,³ Jeffrey W. Baldwin,¹ Steven W. Liskey,¹ Aaron D. Edmunds,¹ William B. Wilson,¹
Michael A. Boone ⁴, Gregory Yesner ¹, Douglas M. Photiadis,¹ and Bernard R. Matis ¹

¹*U.S. Naval Research Laboratory, Physical Acoustics Branch, Washington, DC 20375, USA*

²*The Catholic University of America, Department of Mechanical Engineering, Washington, DC 20064, USA*

³*U.S. Naval Research Laboratory, Acoustic Signal Processing and Systems Branch, Washington, DC 20375, USA*

⁴*Jacobs Engineering, Hanover, Maryland 21076, USA*



(Received 22 February 2022; revised 24 June 2022; accepted 3 August 2022; published 12 August 2022)

Dirac points in the band structure of acoustic systems are essential features affording classical analogs of quantum condensed matter states. We show that measured dispersion curves near and at the Dirac point of an acoustic graphene analog can be suppressed by strong variations in the impedance boundary between free field and surface wave regimes under certain conditions. Increased Rayleigh scattering and diffractive excitation are shown to increase the dispersed surface wave pressure amplitude, circumventing the impedance-based wave suppression. The improved excitation and scattering conditions for observing acoustic Dirac points for two samples with two distinct operational frequency ranges are reported.

DOI: [10.1103/PhysRevB.106.064301](https://doi.org/10.1103/PhysRevB.106.064301)

I. INTRODUCTION

Acoustic analogs of condensed-matter systems [1,2] provide a unique opportunity to conduct experimental studies of various phenomena without the difficulty of working with atomic-scale components, the limitations manifested by inter-particle interactions, or the difficulty of obtaining certain experimental parameters, such as extreme external pressure [3]. These acoustic systems have served as adequate platforms for studying acoustic versions of Landau quantization [4], Klein tunneling [5], *Zitterbewegung* (trembling motion) [6,7], topologically disordered states [4], and extremal transmission [7]. Theoretical studies of multilayer acoustic systems governed by Dirac and Moiré physics [8–10] show promise in the development of acoustic analogs of novel phases of matter such as two-dimensional (2D) superconductivity [11], correlated insulators [12], and nondisorder driven localization [13]. Recent efforts have demonstrated an acoustic analog of graphene through direct band-structure measurements and first principle modeling of acoustic surface waves (ASW) propagating across hexagonal arrays of scatterers [1,2,14–16]. Such systems can have strongly varying boundary conditions, in particular the complex acoustic impedance between the free field and ASW regimes above the lattice elements; the influence of such strongly varying boundary conditions on ASW propagation and measured dispersion relations is not understood.

In this article, we investigate both experimentally and numerically the influence of strongly varying boundary conditions on the measured dispersion of an acoustic graphene analog consisting of a hexagonal lattice of half-open cylindrical cavities and demonstrate that in certain circumstances the

boundary conditions can suppress ASW excitation (i.e., the amount of energy transferred to the ASW regime does not promote measurable dispersion at certain frequencies). The same graphene analog is studied with two samples consisting of different cavity depths, which only affects the operational frequency band of the ASW (the band structure remains the same). This enables direct analysis of the frequency-dependent aspects of ASW measurements. The operational frequency band of an ASW extends to the free-space sound line at frequencies above and below the Dirac frequency.

Using a grazing incidence ASW excitation method [1] combined with a line-scan measurement technique, we find that for certain operational frequency bands ASW suppression occurs near and at the Dirac frequency, which a finite-element model shows is the result of a four-order-of-magnitude variation in the complex impedance boundary condition between the free field and ASW regimes across the lattice's unit cell. Performing the same experiment on a sample where the cavity resonance frequency f_r is a factor of 1.7 higher shifts the operational frequency band to higher frequencies. The corresponding increase in the cavity scattering parameter kr (where k is the wave number and r is the cavity radius), and the level of Rayleigh scattering (acoustic wavelength λ is at least a factor of 10 greater than r), results in greater dispersed ASW pressure amplitude and circumvents the ASW suppression observed in the lower f_r sample. This supports the conclusion that the observed ASW suppression is driven by the strongly varying impedance boundary condition targeted by the grazing incidence excitation method and not specifically the method itself.

We further contrast these results to experiments utilizing a diffraction-based excitation method [2], which couples the incident energy to the ASW via a smoothly varying impedance boundary within a single cavity, and we demonstrate that

*nicholas.gangemi@nrl.navy.mil

this method circumvents the observed ASW suppression at all frequencies considered in our experiments. We note that changing the ASW excitation method allows us to systematically target each boundary condition existing between the free field and ASW regimes, allowing us to elucidate the previously unreported effect of the ASW boundary conditions on the measured dispersion curves. We further contrast these results to a phase delay measurement technique [1], which we find fails to provide access to the Dirac point and allows us to thoroughly describe the most appropriate experimental conditions (excitation method and measurement technique) for observing the Dirac point across operational frequency bands. These findings provide novel and relevant information necessary for advancing the burgeoning field of “acoustic wistronics” [9,10].

II. MATERIALS AND METHODS

A. Acoustic graphene analog samples

Two samples were 3D printed from an acoustically rigid thermoplastic; an image of one of the samples is shown in Fig. 1(a). The samples were fixed to precision ground aluminum plates in order to keep the surface of interest as flat as possible throughout the experiments. The opening of each cavity is partially baffled due to the proximity of the adjacent cavities; however, we find that f_r is well approximated by assuming the cavities are fully baffled. Given a cylindrical cavity, closed on one end, and fully baffled on the open end, f_r is calculated with end corrections as follows [17]:

$$f_r = \frac{n}{4L + (8/3\pi)r}c, \quad (1)$$

where $c = 342$ m/s is the measured free field sound speed, L is the cavity depth of the sample of interest, $r = 1.473$ mm is the cavity radius, and $n = 1$ corresponds to the fundamental cavity resonance frequency. The cavity depths used in our experiments, specifically $L = 2.83$ mm and $L = 5.65$ mm, correspond to cavity resonance frequencies $f_r = 20.9$ kHz and $f_r = 12.4$ kHz, respectively; henceforth, the samples will be identified by their cavity resonance frequencies. Both r and the lattice vector magnitude $|a_1| = |a_2| = 5.78$ mm [Fig. 1(a)] are the same for each sample.

B. Experimental

Each sample was held in place with a kinematic locating system, which ensured repeatability in sample placement relative to the source and receiver throughout the experiments. The band structures were experimentally measured by exciting ASWs across the sample and recording the time series at $n = 20$ discrete locations spaced $\Delta x = 1$ mm apart along the sample’s centerline direction \hat{x} [yellow arrow in Fig. 1(a)] at a height $h = 1.00$ mm above the sample’s surface. This process was automated by fixing the receiver to a precision 3-axis translational platform capable of stepwise displacements as low as $\Delta x = 0.01$ mm. Dispersion information was obtained via the 2D spatial fast Fourier transform (FFT) of this line scan and compared to a finite-element modeling (FEM) eigenfrequency study. The ASWs were excited at both grazing incidence [Fig. 1(b)] [1] and by diffractively coupling

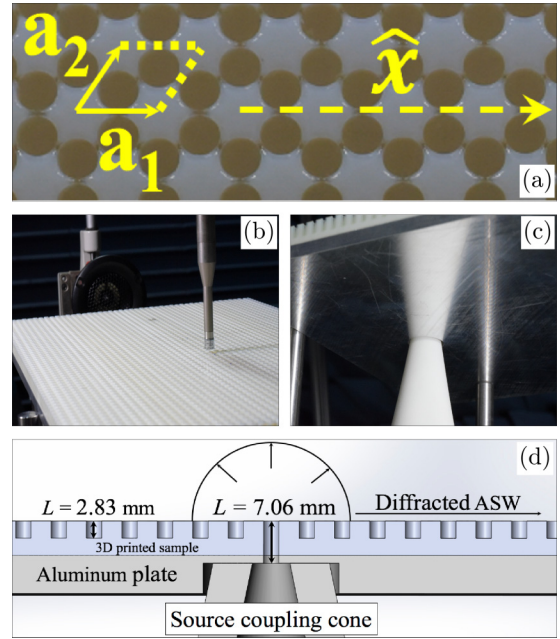


FIG. 1. Sample, experimental setup, and excitation details. (a) Photograph of the 3D printed hexagonal lattice. The lattice unit cell is indicated by the dotted yellow lines and the lattice vectors a_1 and a_2 . The direction of microphone displacement used for the line scan measurement technique is indicated by the unit vector \hat{x} and the dashed yellow arrow. The dark, circular regions are the half-open cylindrical cavities. (b) Photograph of the sample with a cavity resonance frequency $f_r = 20.9$ kHz. The measurement microphone is suspended vertically above the sample. The source, configured for the grazing incidence excitation method, is shown behind the sample. (c) Photograph of the 3D printed cone (white) coupled to the source cavity used for the diffractively coupled excitation method as depicted in the cross-sectional image shown in (d). (d) Cross-sectional schematic of the diffractively coupled excitation method. Here sample dimensions are provided for the sample with $f_r = 20.9$ kHz. The source cavity ($L = 7.06$ mm) is open on both ends and has a resonance frequency ($f_r = 20.9$ kHz) equal to the resonance frequency of the half-open cylindrical cavities ($L = 2.83$ mm) comprising the hexagonal lattice.

the source to the bottom of a single cavity open on both sides [Figs. 1(c) and 1(d)] [2]. For each sample, the length of the source cavity for the diffractively coupled excitation method was designed such that its resonance frequency matches that of the half-open cavities, minimizing any interruption of the lattice’s periodicity; Fig. 1(d) depicts a source cavity depth of $L = 7.06$ mm for the $f_r = 20.9$ kHz sample. We also evaluate dispersion curves obtained by measuring the phase delay of signals [1] recorded at two locations x_1 and x_2 where $x_{12} = 86.45$ mm is the distance between the two microphone locations. Additional experimental information can be found in Appendices A and B.

III. BAND STRUCTURE SIMULATIONS

FEM simulations of the unit cell depicted in Fig. 1(a) were performed using *COMSOL Multiphysics*, version 5.6, to predict the ASW band structure for each sample (Fig. 2).

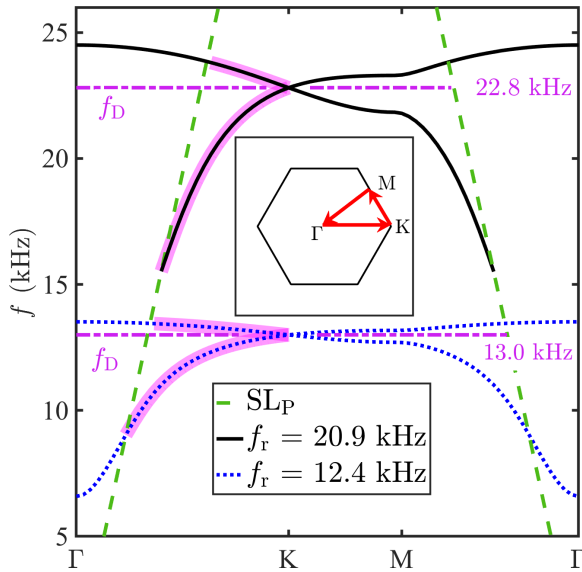


FIG. 2. FEM-predicted band structures and sound lines for the two samples with cavity resonance frequencies $f_r = 20.9$ kHz (solid black line) and $f_r = 12.4$ kHz (dotted blue line), which correspond to Dirac frequencies $f_D = 22.8$ kHz and $f_D = 13.0$ kHz (dot-dashed purple lines), respectively. The regions of each band structure highlighted in magenta are the regions targeted by our experiments; these highlighted predictions are shown as magenta dots in Figs. 3, 5, 8 for comparison to the experimental data. The dashed green lines are the predicted sound lines (SL_P) using $c = 342$ m/s as the air wave speed [note that the measured sound lines (SL_M) are shown as solid green lines in Figs. 3, 5, 8]. Inset: The red arrows indicate the path around the irreducible Brillouin zone taken by sweeping the values of wave-number pairs k_x, k_y during the band-structure eigenfrequency computation.

Most of the air in the cavities and above the surface was modeled using the modules “pressure acoustics” and “frequency domain” with “thermally conducting” and “viscous losses” included. To more accurately approximate for the experimental boundary conditions near the solid surfaces, the thermoviscous acoustics, frequency domain, module was used to apply “no slip” and “isothermal” boundary conditions at walls (i.e., solid surface and cavity surfaces); this region extended approximately 9.2 viscous boundary layers from the walls. The Dirac frequency f_D was chosen to calculate the viscous boundary layer thickness. The air region above the surface extended 13 mm above the thermoviscous layer and was terminated with user defined Port boundary conditions to model a semi-infinite fluid domain above the surface. The periodic boundary conditions were modeled using Floquet periodicity. The eigenfrequency study used the region search method, 11–25 kHz and 6–14 kHz, for the samples with $f_r = 20.9$ kHz and $f_r = 12.4$ kHz, respectively. To calculate the band-structure eigenfrequencies, wave-number pairs (k_x, k_y) were swept along a path outlining an irreducible Brillouin zone, Γ -K-M- Γ (see the Fig. 2 inset). The K point was on the k_x axis ($\theta = 0^\circ$) and the M point was $\pi/6$ radians above the k_x axis. The calculated eigenfrequencies and wave-number pairs were exported to MATLAB for postprocessing and plotting.

Figure 2 depicts the FEM-predicted band structures for $f_r = 20.9$ kHz (solid black line) and $f_r = 12.4$ kHz

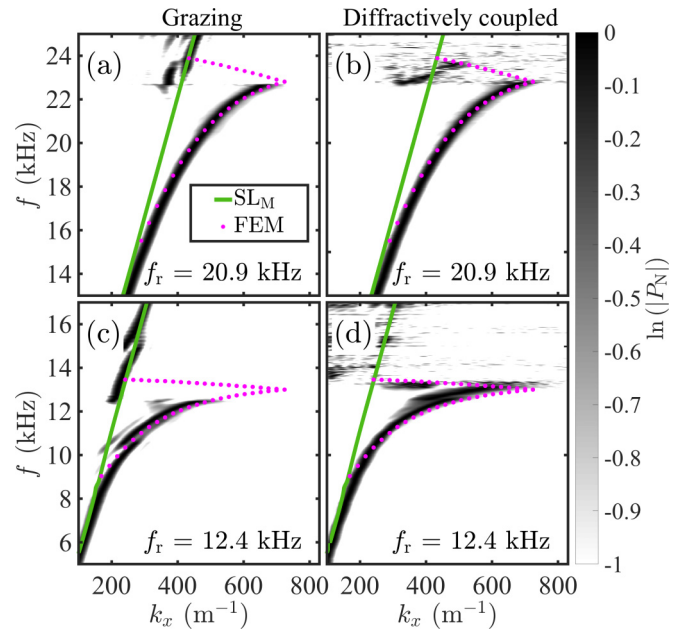


FIG. 3. Frequency-dependent surface wave suppression near and at the Dirac point. All dispersion curves (grayscale) are obtained via the line scan measurement technique. The green lines represent the measured sound line (SL_M) and the magenta dots are the FEM predicted band structure along the \hat{x} direction (a) Cavity resonance $f_r = 20.9$ kHz excited with the grazing incidence excitation method. (b) Cavity resonance $f_r = 20.9$ kHz excited with the diffractively coupled excitation method. (c) Cavity resonance $f_r = 12.4$ kHz excited with the grazing incidence excitation method. (d) Cavity resonance $f_r = 12.4$ kHz excited with the diffractively coupled excitation method.

(dotted blue line). Note that the regions of the predicted band structures highlighted in magenta indicate the regions of the band structures targeted by our experiments; these highlighted predictions are shown as magenta dots in Figs. 3, 5, 8. For each f_r , FEM predicts a Dirac point where the upper and lower branches of each band-structure cross at the K point at the edge of first Brillouin zone (Fig. 2 inset). The Dirac frequencies corresponding to each Dirac point $f_D = 22.8$ kHz ($f_r = 20.9$ kHz) and $f_D = 13.0$ kHz ($f_r = 12.4$ kHz) are indicated with dash-dotted purple lines in Fig. 2. The theoretical sound line corresponding to nondispersed wave propagation through air at a wave speed $c = 342$ m/s is shown as a dashed green line. The FEM-predicted band structures shown in Fig. 2 are in qualitative agreement with previous analogous band-structure predictions [1,2].

IV. RESULTS AND DISCUSSION

A. Measured dispersion curves

Figures 3(a)–3(d) depicts the dispersion curves measured by exciting the samples with Gaussian first derivative pulses centered at $f_c = 24$ kHz [Figs. 3(a) and 3(b)] and $f_c = 16$ kHz [Figs. 3(c) and 3(d)]; these short time excitations were chosen because their center frequencies and wide bandwidth ensures that both f_r and the predicted f_D are within the experimental frequency bands. Here $P_N = P_{\text{rms}}/P_{\text{max}}$, where

P_{rms} is the FFT pressure magnitude and P_{max} is the maximum FFT pressure magnitude obtained for a given frequency. Figure 3(a) shows the dispersion curve measured using the $f_r = 20.9$ kHz sample with the grazing incidence excitation method and the line scan measurement technique. The experimentally obtained wave number (grayscale) for energy nearest to the predicted Dirac point is $k_x = 723 \text{ m}^{-1} \pm 5 \text{ m}^{-1}$, which agrees with the theoretical (magenta) $k_x = \frac{4}{3}\pi(|\vec{a}_1|)^{-1} = 724 \text{ m}^{-1}$ and occurs at $f = 22.7$ kHz (predicted $f_D = 22.8$ kHz), where the upper and lower branches of the band structure touch at the edge of the first Brillouin zone (BZ). Deviation from the measured sound line (SL_M), which is plotted as a solid green line, indicates that the Dirac point is also represented by the slowest traveling surface wave frequency constituent, and we observe a Dirac point phase velocity $v = 197 \text{ m/s} \pm 2 \text{ m/s}$, which is equivalent to the FEM prediction of $v_D = 198 \text{ m/s}$. When the measurement band is lowered by decreasing f_r [Fig. 3(c)], we measure a maximum wave number $k_x = 541 \text{ m}^{-1} \pm 5 \text{ m}^{-1}$ and minimum phase velocity $v = 145 \text{ m/s} \pm 2 \text{ m/s}$, and these values disagree with the theoretical maximum wave number $k_x = 724 \text{ m}^{-1}$ and corresponding Dirac point phase velocity $v_D = 113 \text{ m/s}$. Thus, we conclude that grazing incidence does not excite a fully dispersing ASW in the $f_r = 12.4$ kHz frequency band and does not allow for measurement of the Dirac point.

By using a 3D printed rigid cone to couple the source to the bottom of a single cavity open on both sides, we can excite ASWs via diffraction from the cavity opening at the surface. For the $f_r = 20.9$ kHz sample, exciting the ASW with this technique [Fig. 3(b)] yields an experimentally obtained Dirac point wave number (grayscale) $k_x = 723 \text{ m}^{-1} \pm 5 \text{ m}^{-1}$ in agreement with the FEM (magenta) predicted $k_x = 724 \text{ m}^{-1}$. Likewise, these values of k_x and v ($198 \text{ m/s} \pm 2 \text{ m/s}$) are observed at $f = 22.8$ kHz (predicted $f_D = 22.8$ kHz) where the upper and lower branches meet, indicating successful measurement of the Dirac point. For the $f_r = 12.4$ kHz sample, this excitation technique yields a Dirac point wave number $k_x = 725 \text{ m}^{-1} \pm 5 \text{ m}^{-1}$ and minimum Dirac point phase velocity $v = 114 \text{ m/s} \pm 1 \text{ m/s}$ in agreement with the prediction [Fig. 3(d)]. These values indicate successful observation of the Dirac point at $f = 13.1$ kHz (predicted $f_D = 13.0$ kHz) is achieved in this frequency band with the diffractively coupled excitation method despite the failure of the grazing incidence excitation method to excite a fully dispersed ASW in this same frequency band. Note that the pressure amplitude observed in Figs. 3(b) and 3(d) near the sound line and for $f > f_D$ is associated with wave numbers in the second Brillouin zone and is discussed later in more detail. Additionally, the complete absence of the upper branch in Figs. 3(a) and 3(c) and the partial resolution of the upper branch in Figs. 3(b) and 3(d) has been observed in both sound-based [2] and microwave-based [18] graphene analogs and results from a vanishing Fourier transform integral due to asymmetric pressure distributions above the lattice cavities.

B. Cavity impedance predictions

The failure of grazing incidence to excite ASW modes near and at the Dirac point in the lower-frequency band [Fig. 3(c)] is explained through a combination of the effects of

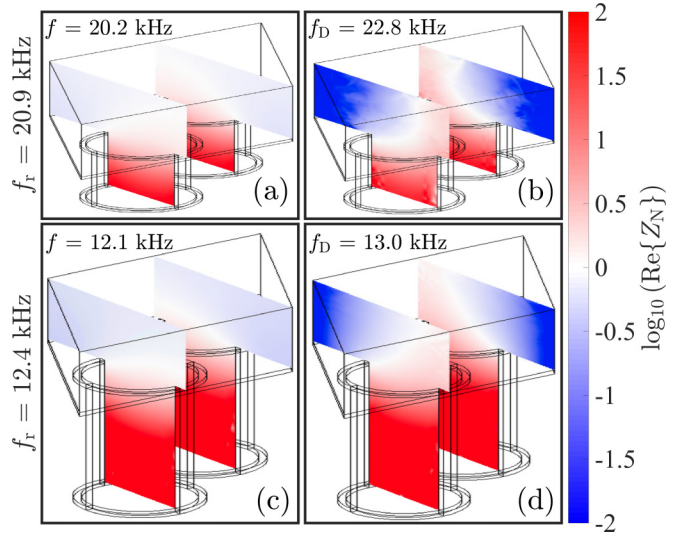


FIG. 4. FEM predictions of the real part of the normalized specific acoustic impedance $Z_N = Z/Z_0$ (colorscale) in and above unit cell cavities. (a) Impedance prediction for cavity resonance $f_r = 20.9$ kHz at $f = 20.2$ kHz. (b) Impedance prediction for cavity resonance $f_r = 20.9$ kHz at the Dirac frequency $f_D = 22.8$ kHz. (c) Impedance prediction for cavity resonance $f_r = 12.4$ kHz at $f = 12.1$ kHz. (d) Impedance prediction for cavity resonance $f_r = 12.4$ kHz at the Dirac frequency $f_D = 13.0$ kHz.

the impedance boundary condition targeted by this excitation method and reduced dispersion due to frequency-dependent Rayleigh scattering. Using FEM, we have computed the complex specific acoustic impedance Z in and above the cavity's unit cell up to $h = 3.00$ mm (a factor of three greater than the microphone height used in the line scans). Figure 4 depicts the real part of the FEM-predicted normalized acoustic impedance magnitude $Z_N = Z/Z_0$, where $Z_0 = 418 \text{ Pa s/m}$ is the characteristic impedance of air (FEM predictions for the imaginary part of the normalized specific impedance can be found in Appendix C). The logarithmic colormaps in Figs. 4(a) and 4(c) plot Z_N at $f = 20.2$ kHz and $f = 12.1$ kHz for $f_r = 20.9$ kHz and $f_r = 12.4$ kHz, respectively (well below f_D for each sample). These colormaps show that grazing acoustic waves are impedance matched to ASW modes at these frequencies because $\log_{10}(\text{Re}\{Z_N\})$ is very close to zero across the unit cell. This explains why an accurate dispersion curve is obtained when f is sufficiently less than f_D yet still within the measurement frequency band. Contrarily, the logarithmic colormaps in Figs. 4(b) and 4(d) predict a four-order-of-magnitude variation in the complex impedance magnitude across the unit cell at $f = f_D$. This supports the conclusion that the absence of the Dirac point and nearby portions of the lower branch of the dispersion curve in Fig. 3(d) is the result of the strongly varying impedance boundary condition across the unit cell at $f = f_D$, which is targeted by the grazing incidence excitation method.

Despite poor impedance coupling between the free field and ASW regimes under the grazing incidence excitation method, the successful measurement of the entire lower branch up to and including the Dirac point with this excitation method for $f_r = 20.9$ kHz [Fig. 3(a)] is explained by a larger cavity scattering parameter kr occurring in this higher

measurement frequency band, which scatters more of the incident energy into the ASW regime. The cavity radius $r = 1.473$ mm is the same for both the $f_r = 20.9$ kHz and $f_r = 12.4$ kHz samples. Given that f_r influences f_D and the measurement band, we obtain $kr = 0.617$ and $kr = 0.349$ at each sample's respective f_D ; note that both values of kr are within the Rayleigh scattering regime because λ is at least a factor of 10 greater than r . For the $f_r = 20.9$ kHz sample, the relatively higher scattering parameter $kr = 0.617$ suggests more energy will be scattered into the ASW regime resulting in an ASW pressure amplitude sufficient for measuring a dispersion curve up to and including the Dirac point; this explains our ability to observe the Dirac point under grazing incidence excitation in the higher-frequency band [Fig. 3(a)] despite the failure of the excitation method to excite a fully dispersed ASW in the lower-frequency band [Fig. 3(c)] due to the varying impedance boundary condition. For $f_r = 12.4$ kHz, $kr = 0.349$ indicates a scattering parameter that is 43.4% less than that of the $f_r = 20.9$ kHz sample. This relatively lower kr is enough to prevent a fully dispersed ASW mode from being excited when coupled with the strongly varying impedance boundary condition under grazing incidence excitation as not enough energy is scattered into the ASW regime and remains in the free field. These results establish the grazing incidence excitation method as a viable excitation method only when f_r , f_D , and thus the measurement band dictate a sufficiently large cavity scattering parameter.

As shown in Fig. 4, the diffractively coupled excitation method targets a smoothly varying boundary condition between the free field and ASW regimes because it targets the air within a single cavity. The colormaps depict a smooth impedance transition from $Z_N = 100$ at the bottom of the cavity (red) to approaching Z_0 at the ASW side of the cavity. By coupling the source to the bottom of a single, open-ended cavity using a gradually tapered cone we minimize the effect of any abrupt impedance transition between the free field and ASW regimes, which maximizes the amount of energy transmitted through the cavity opening and into the ASW regime. As demonstrated by the data shown in Fig. 3(d), the diffractively coupled excitation method yields a successful measurement of the lower branch up to and including the Dirac point for $f_r = 12.4$ kHz, circumventing the suppression of the ASW mode that occurs when the grazing incidence excitation method is used. Successful measurements of the entire lower branch including the Dirac point across frequency bands establishes the diffractively coupled excitation method as a more reliable excitation method for studying ASW propagation over an acoustic graphene analog.

C. Comparing line scan and phase delay measurement techniques

Previous studies [1] have attempted to measure an ASW dispersion curve (up to and including the Dirac point) by means of a phase delay measurement of the ASW at two locations. Here, having demonstrated Dirac point access in both frequency bands using the diffractively coupled excitation method, we use this method to compare dispersion curves obtained with a phase delay measurement technique to those obtained via a line scan measurement technique. We also

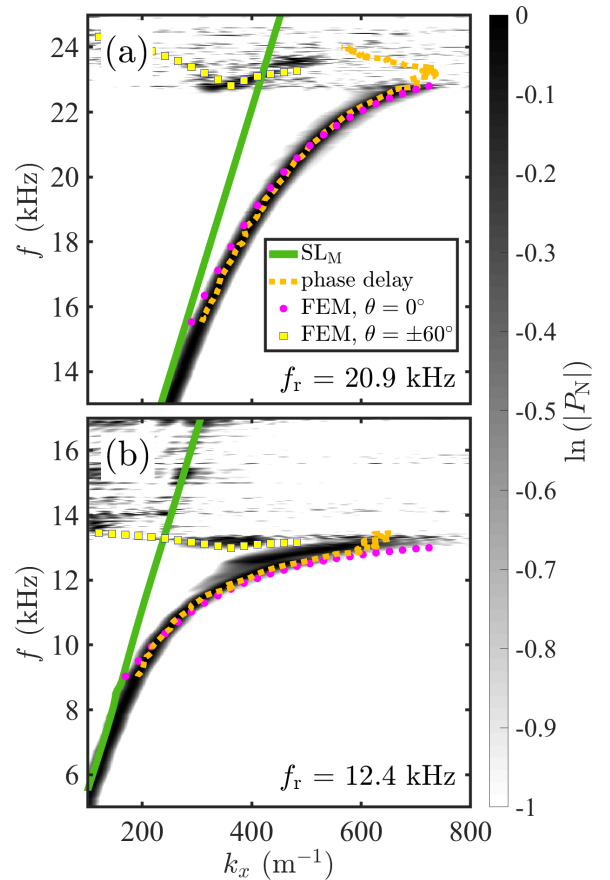


FIG. 5. Comparison of the line scan and phase delay measurement techniques and higher Brillouin zone FEM predictions. The diffractively coupled excitation method is used in each case. Dispersion curves obtained with a line scan are shown in grayscale, and these are the same datasets shown in Figs. 3(b) and 3(d). Dispersion curves obtained with the two point phase delay measurement technique are indicated by the dotted orange line. The green lines represent the measured sound line (SL_M). The magenta dots are the FEM predicted band structure along the \hat{x} direction ($\theta = 0^\circ$), and these are the same predictions shown in Figs. 3(b) and 3(d). The yellow squares are the FEM predicted band structure for $\theta = \pm 60^\circ$ with respect to \hat{x} . (a) Dispersion curves obtained for the $f_r = 20.9$ kHz sample. A phase shift of -6π is required for the phase delay measurement. (b) Dispersion curves obtained for the $f_r = 12.4$ kHz sample. A phase shift of -4π is required for the phase delay measurement.

highlight that certain experimental conditions could prevent a line scan measurement from being performed (specifically in the case of multilayer acoustic systems with only a rotational degree of freedom) and thus a phase delay measurement could be warranted in certain experiments, which motivates the comparison between the line scan and phase delay techniques for measuring an acoustic graphene analog's band structure. Figure 5(a) compares the line scan data and FEM prediction shown in Fig. 3(b) to the results of a two-point phase delay measurement (orange) for the $f_r = 20.9$ kHz sample. The values of k_x for the two-point phase delay measurement are calculated as follows [1]:

$$k_x = \frac{|\Delta\phi|}{x_{12}}, \quad (2)$$

where $\Delta\phi$ is the measured unwrapped phase delay between the two measurement locations, $x_{12} = 86.45$ mm is the distance between the two measurement locations, and $\cos(\theta) = 1$. With the phase delay measurement technique, we calculate $k_x = 703.0 \text{ m}^{-1} \pm 0.1 \text{ m}^{-1}$ at $f_D = 22.8$ kHz (the predicted Dirac frequency), which is 2.77% less than $k_x = 723 \text{ m}^{-1} \pm 5 \text{ m}^{-1}$ measured with a line scan and verified with FEM. The largest wave number measured with the phase delay measurement technique is $k_x = 737.0 \text{ m}^{-1} \pm 0.1 \text{ m}^{-1}$, which occurs at a frequency slightly higher ($f = 23.2$ kHz) than the predicted f_D .

Similar observations are made with the $f_r = 12.4$ kHz sample. Figure 5(b) shows that we measure $k_x = 628.0 \text{ m}^{-1} \pm 0.1 \text{ m}^{-1}$ at $f_D = 13.0$ kHz (the predicted Dirac frequency) with the phase delay technique, which is 9.66% less than the line scan results where $k_x = 725 \text{ m}^{-1} \pm 5 \text{ m}^{-1}$. If we consider the maximum observed wave number from the phase delay measurement $k_x = 655.0 \text{ m}^{-1} \pm 0.1 \text{ m}^{-1}$ to represent the Dirac point, then the frequency at which this maximum occurs (13.3 kHz) disagrees with the Dirac frequency $f_D = 13.0$ kHz, which was predicted with FEM and confirmed with the line scan measurement technique. The results of these phase delay measurements demonstrate the inherent limitations of using this measurement technique to accurately measure ASW dispersion information for frequencies near and at f_D in both operational frequency bands considered. A direct comparison to the results obtained in Ref. [1], which uses a grazing incidence excitation method and a phase delay measurement technique, can be found in Appendix D.

Additionally, it is important to note that two-point phase delay measurements are inherently susceptible to arbitrary phase shifts in multiples of 2π . Dispersion curves measured with a phase delay-based approach could require a phase shift to be applied in post processing so that the dispersion information is presented and interpreted correctly. For this reason, a measured reference (in our case the sound line) is always required to ensure the correct phase shift is being applied. In the case of the phase delay measurements shown in Fig. 5, phase shifts of -6π ($f_r = 20.9$ kHz) and -4π ($f_r = 12.4$ kHz) were applied to the orange curves in Fig. 5(a) and Fig. 5(b), respectively, in order to directly and accurately compare them to both the dispersion curves obtained by the FEM simulation and those measured with the line scan technique. Also, it has been shown that attenuation of the ASW can yield a poor signal to noise ratio for frequencies at and above f_D [2], which can lead to nontrivial errors in the phase unwrapping; such unwrapping errors will require different phase shifts to be applied within each narrow frequency band in order to obtain the most accurate dispersion information. This necessitates an accurate reference for each frequency band requiring its own phase shift if band structures obtained with the two-point phase delay measurement technique are to be accurately interpreted.

D. Energy in higher-order Brillouin zones

Last, we compare the portions of the measured dispersion curves in Fig. 5 for $f > f_D$ and close to the sound line [in Fig. 5(a) this energy appears to cross the sound line], which extends from $k_x \sim 315 \text{ m}^{-1} \pm 5 \text{ m}^{-1}$ to $k_x \sim 435 \text{ m}^{-1} \pm 5 \text{ m}^{-1}$, to the FEM predicted upper branch in the

second BZ along a vector at an angle $\theta = \pm 60^\circ$ with respect to \hat{x} (solid yellow squares). The agreement between the FEM prediction and the data at these frequencies indicates the measurement of an \hat{x} component of a higher-order BZ band structure along the $\theta = \pm 60^\circ$ direction (corresponding to the branch between the M and K critical points). The measured data in this frequency range is ultimately a superposition of multiple higher-order BZ \hat{x} components; however, we have provided the FEM prediction for a single angle ($\theta = \pm 60^\circ$) to illustrate that portions of the band structure in higher-order BZs are observable with the diffractively coupled excitation method and the line scan measurement technique. This excitation method excites an ASW uniformly in all directions, affording observation of portions of the band structure along different angles due to the tracing of these components to the \hat{x} direction. Contrarily, these portions of the band structure are not observable with an excitation at grazing incidence [confirmed in Figs. 3(a) and 3(c)] as the source is oriented along \hat{x} and thus excites an ASW predominantly in this direction.

V. CONCLUSION

We have studied the effects of strongly varying impedance boundary conditions on ASW dispersion in an acoustic graphene analog and have found that the effects are non-negligible and can suppress ASW excitation in certain frequency bands under certain experimental conditions. Our results demonstrate that increased Rayleigh scattering can circumvent the observed ASW suppression, which is accomplished in our experiments when the frequency band is increased. Ultimately, our results show that a diffractively coupled excitation method, which targets a smoothly varying boundary condition between the free field and ASW regimes, combined with a line scan measurement technique is the most reliable experimental platform for measuring the ASW dispersion curve. Further, our results advance the state of the art in acoustic analogs of condensed matter systems by providing a deeper understanding of boundary condition-driven energy loss, which is pivotal for the realization and characterization of multilayer acoustic analogs of condensed matter physics systems.

ACKNOWLEDGMENTS

This work was funded by the Office of Naval Research. The authors acknowledge Alain Berdoz, Michael Saniga, and Philip Frank for their contributions regarding installation, maintenance, and operation of our measurement system.

APPENDIX A: EXPERIMENTAL SETUP DETAILS

The ASWs were excited using a Beston round ribbon tweeter loudspeaker of diameter $d_s = 25.4$ mm as the source for both the grazing incidence and diffractively coupled excitation methods. The receiver is a precision measurement condenser microphone of capsule diameter $d_r = 6.35$ mm, and calibrated to $f = 100$ kHz. Before digitization, measured signals were amplified and filtered using an Ithaco 1201 low-noise preamplifier with a gain of 20 and a passband of 3 kHz $< f < 100$ kHz. For the grazing incidence excitation method

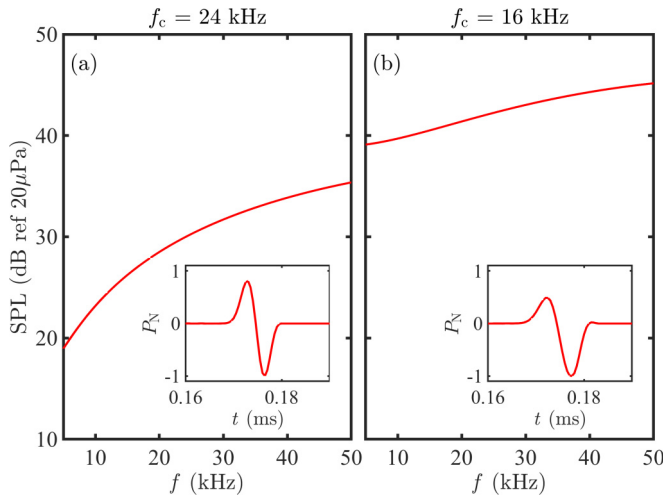


FIG. 6. Measured spectral content of Gaussian first derivative waveforms used to excite the ASWs. (a) Waveform centered at $f_c = 24$ kHz. Inset: Amplitude normalized time series of the waveform where $P_N = P/P_{\max}$. (b) Waveform centered at $f_c = 16$ kHz. Inset: Measured amplitude normalized time series of the waveform where $P_N = P/P_{\max}$.

[Figs. 3(a) and 3(c)], the source is positioned $x = 64.30$ mm away from the sample's leading edge, and aligned such that its center axis corresponds to the sample's centerline along the vector \hat{x} [Fig. 1(a)], which is the direction along which the line scan and phase delay measurements were performed. Positioning the source in this manner compensates for the nonuniform directivity pattern that arises when operating in the frequency ranges of our experiments, and ensures sufficient energy is transmitted to the receiver.

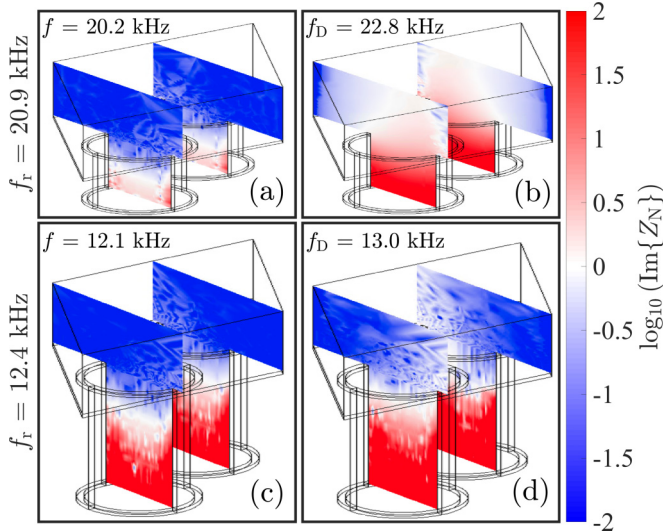


FIG. 7. FEM predictions of the imaginary part of the normalized specific acoustic impedance $Z_N = Z/Z_0$ (color scale) in and above unit cell cavities. (a) Impedance prediction for cavity resonance $f_r = 20.9$ kHz at $f = 20.2$ kHz. (b) Impedance prediction for cavity resonance $f_r = 20.9$ kHz at the Dirac frequency $f_D = 22.8$ kHz. (c) Impedance prediction for cavity resonance $f_r = 12.4$ kHz at $f = 12.1$ kHz. (d) Impedance prediction for cavity resonance $f_r = 12.4$ kHz at the Dirac frequency $f_D = 13.0$ kHz.

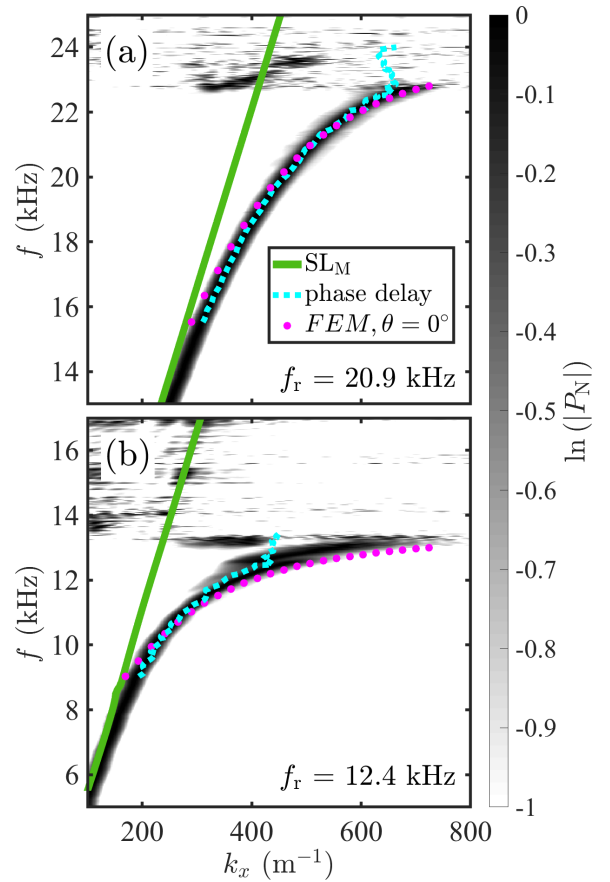


FIG. 8. Line scan with the diffractively coupled excitation method versus phase delay measurement with grazing incidence excitation method. The line scan dispersion curves are shown in grayscale, the phase delay dispersion curves are shown with a cyan dotted line, the green lines represent the measured sound line, the magenta dots are the FEM predicted band structure along the \hat{x} direction ($\theta = 0^\circ$). (a) Dispersion curves obtained for the $f_r = 20.9$ kHz sample. No phase shift is required for this particular phase delay measurement. (b) Dispersion curves obtained for the $f_r = 12.4$ kHz sample. A phase shift of $-\pi$ is required for the phase delay measurement.

For the diffractively coupled excitation method [Figs. 3(b) and 3(d)], a counterbore is made through the aluminum plate, and the bottom of a cavity is opened such that the total cavity length is $L = 7.06$ mm for the $f_r = 20.9$ kHz sample, and $L = 12.7$ mm for the $f_r = 12.4$ kHz sample. The source was mated to the bottom of this cavity via a 3D printed tapered cone, which smoothly transitions from a diameter of $d = 97.68$ mm to $d = 6.40$ mm.

APPENDIX B: EXCITATION WAVEFORMS

Figure 6 depicts the measured spectral content of each excitation signal. The insets are the measured amplitude normalized time series which have been windowed with a cosine-tapered window in order to minimize spectral leakage. Note that the higher sound pressure level in the spectrum corresponding to $f_c = 16$ kHz [Fig. 6(b)] is due to an enhanced speaker response at subultrasonic frequencies. Despite this,

both the $f_c = 24$ kHz and $f_c = 16$ kHz waveforms provide signal amplitude sufficient to excite ASWs across the samples with both the grazing incidence and diffractively coupled excitation methods.

APPENDIX C: IMAGINARY PART OF PREDICTED IMPEDANCE (FEM)

Figure 7 depicts the imaginary part of the FEM-predicted normalized specific acoustic impedance magnitude $Z_N = Z/Z_0$ where $Z_0 = 418$ Pa s/m is the characteristic impedance of air (the real part of Z_N is shown in Fig. 4 in the main text). A four-order-of-magnitude variation in the imaginary part of Z_N is observed in the logarithmic colormaps, which supports the conclusion drawn in the main text that Z varies significantly across the boundary between the free field and ASW regimes.

APPENDIX D: PHASE DELAY MEASUREMENT TECHNIQUE WITH GRAZING INCIDENCE EXCITATION

Prior state-of-the-art measurements in acoustic graphene analog research utilized a grazing incidence excitation method with a two-point phase delay measurement technique to obtain ASW dispersion information [1]. After establishing the diffractively coupled excitation method as applicable to multiple frequency bands, we used this method to compare the line scan measurement technique to the two-point phase delay

measurement technique. In order to compare our experimental line scan results to the results of Ref. [1] we performed additional measurements using the grazing incidence excitation method (the only excitation method used in Ref. [1]) in combination with a two-point phase delay measurement technique (the only measurement technique used in Ref. [1]). Figure 8 shows the same grayscale data (diffractively coupled excitation method with the line scan measurement technique) and FEM predictions (magenta dots) shown in Figs. 3(b) and 3(d) of the main text along with the new results using grazing incidence excitation with a two-point phase delay measurement technique (dotted cyan lines); note, the sound lines are the same as those in the main text.

With the grazing incidence excitation method and the phase delay measurement technique, based on Eq. (2) we calculate $k_x = 653.8 \text{ m}^{-1} \pm 0.1 \text{ m}^{-1}$ at $f_D = 22.8$ kHz (the predicted Dirac frequency), which is 9.57% less than $k_x = 723 \text{ m}^{-1} \pm 5 \text{ m}^{-1}$ measured with the diffractively coupled excitation method and the line scan technique, and verified with FEM [Fig. 8(a)]. This discrepancy between k_x measured with the grazing incidence excitation method and the phase delay measurement technique and k_x measured with the diffractively coupled excitation method and the line scan technique becomes more severe with the $f_r = 12.4$ kHz sample [Fig. 8(b)]. These results suggest that the combination of grazing incidence excitation with a phase delay measurement does not promote observation of the Dirac point.

-
- [1] D. Torrent and J. Sánchez-Dehesa, *Phys. Rev. Lett.* **108**, 174301 (2012).
 - [2] T. A. Starkey, V. Kyrimi, G. P. Ward, J. R. Sambles, and A. P. Hibbins, *Sci. Rep.* **9**, 15773 (2019).
 - [3] S. M. Gardezi, H. Pirie, S. Carr, W. Dorrell, and J. E. Hoffman, *2D Mater.* **8**, 031002 (2021).
 - [4] X. Wen, C. Qiu, Y. Qi, L. Ye, M. Ke, F. Zhang, and Z. Liu, *Nat. Phys.* **15**, 352 (2019).
 - [5] C. W. J. Beenakker, *Rev. Mod. Phys.* **80**, 1337 (2008).
 - [6] M. I. Katsnelson, *Eur. Phys. J. B* **51**, 157 (2006).
 - [7] X. Zhang and Z. Liu, *Phys. Rev. Lett.* **101**, 264303 (2008).
 - [8] H. Pirie, S. Sadhuka, J. Wang, R. Andrei, and J. E. Hoffman, *Phys. Rev. Lett.* **128**, 015501 (2022).
 - [9] M. Rosendo Lopez, F. Peñaranda, J. Christensen, and P. San-Jose, *Phys. Rev. Lett.* **125**, 214301 (2020).
 - [10] Y. Deng, M. Oudich, N. J. R. K. Gerard, J. Ji, M. Lu, and Y. Jing, *Phys. Rev. B* **102**, 180304(R) (2020).
 - [11] Y. Cao, V. Fatemi, S. Fang, K. Watanabe, T. Taniguchi, E. Kaxiras, and P. Jarillo-Herrero, *Nature (Lond.)* **556**, 43 (2018).
 - [12] Y. Cao, V. Fatemi, A. Demir, S. Fang, S. L. Tomarken, J. Y. Luo, J. D. Sanchez-Yamagishi, K. Watanabe, T. Taniguchi, E. Kaxiras, R. C. Ashoori, and P. Jarillo-Herrero, *Nature (Lond.)* **556**, 80 (2018).
 - [13] P. Wang, Y. Zheng, X. Chen, C. Huang, Y. V. Kartashov, L. Torner, V. V. Konotop, and F. Ye, *Nature (Lond.)* **577**, 42 (2020).
 - [14] J. Tizianel, J. F. Allard, and B. Brouard, *J. Acoust. Soc. Am.* **104**, 2525 (1998).
 - [15] W. Zhong and X. Zhang, *Phys. Lett. A* **375**, 3533 (2011).
 - [16] L.-Y. Zheng, V. Achilleos, Z.-G. Chen, O. Richoux, G. Theocharis, Y. Wu, J. Mei, S. Felix, V. Tournat, and V. Pagneux, *New J. Phys.* **22**, 013029 (2020).
 - [17] L. E. Kinsler, A. R. Frey, A. B. Coppens, and J. V. Sanders, *Fundamentals of Acoustics*, 4th ed. (John Wiley & Sons, New York, 2000).
 - [18] Y. N. Dautova, A. V. Shytov, I. R. Hooper, J. R. Sambles, and A. P. Hibbins, *Appl. Phys. Lett.* **110**, 261605 (2017).